Materials and Design 191 (2020) 108610

Contents lists available at ScienceDirect

Materials and Design

journal homepage: www.elsevier.com/locate/matdes

Scalable magnet geometries enhance tumour targeting of magnetic nano-carriers

Matin Mohseni [a,*], John J. Connell [a], Christopher Payne [a], P. Stephen Patrick [a], Rebecca Baker [a], Yichao Yu [a], Bernard Siow [a], May Zaw-Thin [a], Tammy L. Kalber [a], Quentin A. Pankhurst [b], Mark F. Lythgoe [a]

[a] Centre for Advanced Biomedical Imaging, University College London, 72 Huntley Street, WC1E 6DD, United Kingdom
[b] Healthcare Biomagnetics Laboratory, University College London, 21 Albemarle Street, London, United Kingdom

HIGHLIGHTS

- Magnetic tumour targeting of 100 nm iron-oxide nanoparticles was investigated using a range of different magnet designs.
- The bespoke encompassing magnet increased the effective targeting depth when compared to a conventional disk magnet.
- This magnetic setup can be up-scaled to target 100 nm particles up to a depth of 7cm within human body.

GRAPHICAL ABSTRACT

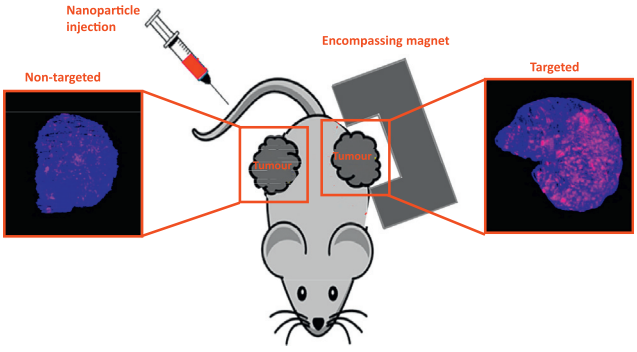

ARTICLE INFO

Article history:
Received 4 November 2019
Received in revised form 14 February 2020
Accepted 27 February 2020
Available online 03 March 2020

Keywords:
Magnetic targeting
Nanoparticles
Magnetic design
Magnetically active space
B.gradB value
Capturing efficiency

ABSTRACT

Targeted drug delivery systems aim to increase therapeutic effect within the target tissue or organ, while reducing off-target toxicity associated with systemic delivery. Magnetic drug targeting has been shown to be an effective strategy by manipulating therapeutics inside the body using a magnetic field and an iron oxide carrier. However, the effective targeting range of current magnets limits this method to small animal experiments or superficial parts of the human body. Here we produce clinically translatable magnet designs capable of increasing exposure of tissue to magnetic fields and field gradients, leading to increased carrier accumulation. The iron oxide nanoparticle capturing efficiency was first assessed in vitro using a simple vascular flow system. Secondly, accumulation of these particles, following magnetic targeting, was evaluated in vivo using a range of different magnet designs. We observed that our bespoke magnet produced a 4-fold increase in effective targeting depth when compared to a conventional 1 T disk magnet. Finally, we show that this magnet is readily scalable to human size proportions and has the potential to target 100 nm particles up to a depth of 7 cm at specific locations of human body.

1. Introduction

One of the current challenges in cancer therapy is delivering a high concentration of drug to the tumour tissue while reducing systemic dosing, thereby limiting off-target adverse effects [1,2]. Magnetic nanoparticles, in combination with applied magnetic field gradients, can

* Corresponding author.
E-mail address: matin.mohseni.15@ucl.ac.uk (M. Mohseni).

https://doi.org/10.1016/j.matdes.2020.108610

increase delivery of small molecule drugs [3] and cells [4–7] to a specific site within the body to enhance their therapeutic effect [8]. Additionally, superparamagnetic iron oxide nanoparticles (SPIONs) can act as magnetic resonance imaging (MRI) contrast agents [8–10], enabling non-invasive imaging of particle delivery to the region of interest, as well as hyperthermia cancer therapy [11], heat triggered drug release [12,13], and mechanical rotation to induce cancer cell death [14]. The multiple actions of biocompatible SPIONs means that they are well-suited for both drug delivery and as diagnostic imaging agents [15].

Previous studies have utilised SPIONs and magnetic field gradients to steer therapeutic cells [16,17] or to deliver drugs [18]. The efficacy of such delivery systems depends on the magnetic content and pharmacokinetic properties of the magnetic carrier such as size and surface composition, as well as the magnet design and depth of the targeting region [8,19]. Larger micron sized carriers are eliminated from the bloodstream by the reticuloendothelial system (RES) faster than nanometre sized particles [8,20]. As a result, much of the magnetic drug targeting literature has focused on developing small, surface modified nanoparticles [21–24] to evade RES and increase blood circulation time as well as increasing extravasation efficiency of the delivery system through the enhanced permeability and retention (EPR) effect - a process by which nano-sized particles leak preferentially into tumour tissue through permeable tumour vessels and are then retained in the tumour bed due to reduced lymphatic drainage [25]. Some of these engineered nanoparticles include surface PEGylated [21] or liposomes-encapsulated particles [22] and other biocompatible formulations [23,24]. However, an important question is whether the applied magnetic field gradient is sufficient to capture such nanoparticles at the target region. A larger net force can be applied to SPION-loaded cells or complex carriers such as heavily SPION-loaded liposomes over individual nanoparticles with a single or multi-domain core, leading to greater targeting efficiency due to their larger size and iron content. This creates a significant challenge for magnetic drug targeting using individual nanoparticles. Nonetheless, Chertok et al. [26] have shown that magnetic targeting using an electromagnet could enhance the delivery of individual nanoparticles to rat brain tumours.

Despite these positive results, clinical studies on magnetic drug targeting [1,2] have been limited, partly due to the poor penetration depth of the magnetic field gradient, resulting in sub-optimal targeting to deeper tissues of the human body. The effective range of currently available electro and permanent magnets limit such a technique to tissues close to the body surface [19]. One benefit of electromagnets is their ability to generate gradients to target SPION loaded cells [27,28] and micron sized particles [29] to deeper locations within the body [30]. However, to date there has been no evidence to suggest that electromagnets can exert magnetic forces strong enough to capture submicron particles at internal organ targets at the clinical scale. Instead, much of the magnetic targeting literature has focused on using simple permanent magnets [1,2,6,16,24] as they are cheap, versatile and do not require a power supply, additional cooling or sophisticated control algorithms. Using finite element methods and theoretical optimisation, we have previously addressed the issue of scalability by designing a permanent magnet system for enhanced magnetic cell delivery to human lower leg arteries [4,16]. With this in mind, we have developed scalable magnetic systems to enhance delivery of individual nanoparticles to tumours in vivo. Compared to a traditional disk magnet, these systems generate a larger region of space with substantial magnetic field gradients; which we refer to as magnetically active space. Such a magnetic setup facilitates deeper body targeting as well as increased nanoparticle delivery throughout the whole tumour.

In this study we investigated magnetic targeting of two sizes of commercially available SPIONs (fluidMAG-CT, Chemicell) under simulated physiological conditions using a capillary flow phantom to determine the effect of flow velocity and nanoparticle size on targeting efficiency. Subsequently, we have shown that the delivery of the same particles can be enhanced in tumours in mice using a static magnetic field after intravenous injection in vivo. This was performed using three different magnet designs: **i) Disk magnet**: a traditional cylindrical permanent magnet; **ii) Magnetic mangle**: a double cylindrical permanent magnet designed to achieve a more uniform exposure of magnetic field gradient compared to a single magnet; and **iii) Pyramid magnet**: a bespoke disk magnet with a pyramidal cavity creating a 3-dimensional exposure of a strong and uniform magnetic field gradient. Additionally, we have applied MRI to quantify local changes in T_2^* relaxation relating to the regional tumour distribution of nanoparticles after magnetic targeting. The targeting results were confirmed by direct iron measurements on ex-vivo tumour tissues. Finally we present a scaled-up magnet capable of targeting particles in tumours located at deep locations in human body.

2. Materials and methods

2.1. Characterisation

2.1.1. Magnet designs

(i) Disk magnet design: A cylindrical neodymium iron boron permanent magnet (1 T residual magnetism, grade N52) with 4.5 cm diameter and 3 cm height. As the highest magnetic field gradient is generated at the edge of the magnet, the magnetic flux density map around the edge of this magnet was simulated in two orthogonal planes (Supplementary Fig. 1) using Opera-3d Cobham Vector Fields simulation software (Oxfordshire, UK). These planes are oriented at 30° from the circular face of the magnet where the vascular flow phantom and the subcutaneous tumours were positioned. The magnetic field gradient map was calculated using MATLAB 2016a (MathWorks, Inc., Massachusetts, US) and the dot product (an algebraic operation of two vectors) of the magnetic field strength and gradient (B.gradB) was plotted (Supplementary Fig. 4A, B) to indicate the magnetic force applied by the magnet. The orientation of the magnet used for the phantom and in vivo experiments are shown in Supplementary Fig. 1A and B respectively. The same edge of the magnet was used for all experiments using this magnet.

(ii) Magnetic mangle design: A magnet design consisting of two cylindrical N42 Neodymium Magnets (20 mm × 20 mm thick diametrically), which are fixed in place with a gap of 14 mm in between them. These magnets are diamatrically magnetised perpendicular to their long axis, and are able to rotate about their long axis. The magnetic field topography in the magnetically active space of these magnets is a function of angle between magnetisation directions of the two magnets. In these experiments, a collinear magnet configuration was used with an N-S-N-S pole arrangement between the two magnets. The magnetic field strength between the magnets was simulated in two orthogonal planes (Supplementary Fig. 2) using Opera Cobham simulation software (Oxfordshire, UK). The magnetic field gradient map was calculated using MATLAB and the B.gradB map was plotted (Supplementary Fig. 4C, D).

(iii) Pyramid magnet: A cylindrical neodymium iron boron permanent magnet (1.45 T residual magnetism, grade N52, similar dimensions to the disk magnet) consisting of a pyramidal hollow space to accommodate the subcutaneous tumour. The pyramidal space has a length and widths of 12 mm and depth of 6 mm. This magnet was designed to produce a strong B.gradB across the tumour. The magnetic flux density map was simulated for a circular surface with diameter 10 mm inside the pyramidal cavity in two orthogonal planes (Supplementary Fig. 3) where the subcutaneous tumours were positioned during magnetic targeting. The magnet is designed and produced by Giamag technologies (Norway). Simulations were made by COMSOL multiphysics software (COMSOL Inc., Sweden).

(iv) Scaled-up magnet: In order to investigate the minimum required B.gradB magnitude to target individual nanoparticles in human tumours, we utilised the results of the phantom targeting experiments and used mathematical modelling to validate these results. The Nacev-

Shapiro model [31] is particularly useful for mathematical validation because it predicts the in vivo efficiency of magnetic targeting based on magnetic, viscoelastic, convective and diffusive forces acting on nanoparticles. We adopted the required parameters and mathematical calculations from Al-Jamal et al magnetic drug targeting paper [24], which adopted blood and blood vessel parameters from the clinical magnetic drug targeting paper [1]. The model calculations predicted a successful magnetic targeting of 100 nm particles for the projected human model using our threshold B.gradB value (see the supplementary information and Supplementary Fig. 8). Using such B.gradB value as the minimum strength requirement, we worked with the Giamag technologies to design a scaled-up magnetic array, which is feasible for assembly and production.

2.1.2. Magnetic nanoparticles

The magnetic nanoparticles used in this study were fluidMag-CT, 100 nm and 50 nm diameters, with a magnetite core and carboxyl functional group coating (Chemicell®, Berlin, Germany). All experiments were performed using the same batch of nanoparticles. In order to characterise these particles, Dynamic Light Scattering (DLS) and Transmission electron microscopy (TEM) images of these particles were acquired at 25 °C with particles resuspended in ddH_2O and at 173° scattering angle for the DLS. The characterisation data was reported in Supplementary Fig. 5. The nanoparticle solution is diluted in PBS, which is buffered to pH 7.4. This was used in all experiments.

2.2. Flow phantom simulation of magnetic targeting

2.2.1. Vascular flow phantom

A phantom flow experiment was used to simulate magnetic targeting of iron oxide nanoparticles in a simplified model. A standard configuration consisting of the magnet and a 0.38 mm internal diameter capillary tube (Smiths Medical Ltd., UK) was used. A solution containing 0.4 mg of fluidMag-CT particles was diluted with 1.5 mL of PBS (typical mouse blood volume) and infused into the tube using an infusion pump (PHD 2000 Harvard Apparatus, US). Physiologically relevant capillary blood flow velocities were chosen based on the values used in previous in vitro studies [31–33] at 5 mms^{-1}, 8 mms^{-1} and 10 mms^{-1} corresponding to flow values of 0.037 mL/min, 0.060 mL/min and 0.075 mL/min respectively. The total infusion volume was kept constant for all experiments. The disk magnet was placed at four distances (0, 3, 6, and 8 mm) from the tube for each flow velocity value. When repeated with the magnetic mangle design, nanoparticles were infused into the tube at the same flow velocities and at 6 distances (0, 3, 6, 8, 11 and 14 mm) relative to one of the magnets.

2.2.2. Quantification using ferrozine assay

The tubes containing accumulated nanoparticles were flushed with 0.6 M hydrochloric acid and placed in a heat block at 65 °C for 2 h. 30 μL of pre-made ferrozine reagent was then added to the samples and the absorbance was measured at 570 nm using a benchtop spectrophotometer (Multiskan™ FC microplate photometer, Thermo scientific). The same procedure was carried out for serial dilutions of known amounts of fluidMag-CT particles to allow calibration (example image Supplementary Fig. 6). The capturing efficiency for each sample was calculated as the percentage of the captured particles over the total perfused mass of particles.

2.3. In vivo magnetic targeting and imaging

2.3.1. Magnetic targeting

All animal studies were approved by the University College London Biological Services Ethical Review Committee and licensed under the UK Home Office regulations and the Guidance for the Operation of Animals (Scientific Procedures) Act 1986 (Home Office, London, UK). Mice ($n = 18$) were subcutaneously injected on each flank with 1×10^6 LS174T colorectal tumour cells (ATCC, CL-188). At no point during the study did any animal show any change in body condition, weight or behaviour from baseline. Once palpable, tumours were measured in three orthogonal dimensions by calipers. Tumour volumes were calculated assuming an ellipsoid shape using the formula [34]:

$$\text{Volume} = \frac{\pi}{6} * L * W * H.$$

Tumour sizes taken at the time of injection for experiments with different magnets are provided in Table 1. Two weeks after cell implantation, anaesthesia was induced and maintained in 1.5–3.0% isoflurane in 1 L/min O_2 and a volume of 100 μL containing 0.4 mg of 100 nm fluidMAG-CT particles (dose of 20 mg/kg) was intravenously injected into the mouse via a tail vein. The magnet was positioned directly over the surface of one of the bilateral tumours during and for 20 min after nanoparticle injection. The spatial profile of the applied magnetic field was varied by utilising three different magnet designs (Supplementary Figs. 1–3) in different experiments while keeping all other experimental procedure the same.

2.3.2. MR imaging

Mice were positioned in a 35 mm Rapid RF coil and maintained at 37 °C with warm water tubing and temperature and respiration monitoring with rectal probe and pressure-sensitive pad (SA instruments Inc.); respiration rate was typically 60–80 bpm. T_2-weighted and T_2^* map images were acquired before and after nanoparticle administration using respiratory-triggered fast spin echo sequence (TR/TE 1000/9 ms, Echo Train Length (ETL) 4, 20 × 1 mm thick slices, 1 average, data matrix 256^2, field of view 30 × 30 mm, ≈1 min) and multiple gradient echo sequence (TR 500 ms, 16 echoes 1.51–27.25 ms, 4 averages, 256^2, 30 × 30 mm, 5 × 1 mm thick slices) using a 9.4 T Varian Inova scanner (Varian, Santa Clara, CA).

For tumours targeted using the magnetic mangle and pyramid magnets, T_2^* map images were acquired before and after magnetic targeting experiment using respiratory-triggered and multiple gradient echo sequences (TR 1500 ms, 5 echoes 5.2–30 ms, 1 average, 192^2, 30 × 30 mm, 1 mm thick slices) using a 1 T Bruker ICON scanner (Bruker, Germany).

In order to perform three-dimensional MRI scan on ex-vivo tumours, tumour samples were fixed in 4% paraformaldehyde overnight. The samples were then placed in a phantom with 1% agar and the phantom was imaged using 3D spoiled gradient echo (SPGR) sequence (TR = 15 ms, TE = 7 ms, matrix = 512 × 512 × 512, FOV = 30 × 30 × 30 mm, total acquisition time = 5 h 27 min. Image resolution was 59 × 59 × 59 μm^3) using the 9.4 T Varian.

2.3.3. Image analysis

The T_2^* maps were measured by mono-exponential fitting of signal decay to each voxel in manually chosen regions of interest (ROIs) using non-linear least squares method in MATLAB. To map the distribution profile of nanoparticle accumulation within tumours, the T_2^* value of line segments located at 1 mm intervals through the tumour were measured for both targeted and non-targeted tumour groups before and after nanoparticle injection ($n = 6$) for each magnet experiment group. This was performed between the ranges of 1 to 4 mm within the tumours. Data were analysed with in-house MATLAB code. The

Table 1
Subcutaneous tumour volumes at the time of injection for experiments with different magnet design (mean ± SD).

Experiment	Targeted (mm^3)	Non-targeted (mm^3)
Disk magnet	109.5 ± 25.9	99.1 ± 38.6
Magnetic mangle	92.5 ± 34.6	106.3 ± 64.5
Pyramid magnet	99.7 ± 31.6	105.5 ± 22.2

results of the two imaging groups (pre and post injection) were statistically tested using non-parametric Wilcoxon test for each tumour group (Targeted and non-targeted).

The 3D images on tumour samples were manually segmented on 3D gradient echo images. Firstly, the intensity values were scaled to between zero and one by dividing by the maximum signal intensities and then thresholding was performed on regions that were less than an arbitrary value chosen to be 0.2. The manually segmented images were then volume rendered using ImageJ software 3D Viewer (Rasband, ImageJ, NIH, Bethesda, Maryland, USA).

2.3.4. Perl's Prussian blue stain

Tumour samples were fixed in 4% paraformaldehyde and then processed for histology, embedded in paraffin wax blocks and sectioned in 5 μm slices. Prior to staining, adjacent sections were cleared in xylene and then rehydrated through 100%, 95% and 50% ethanol to distilled water. The sections were then incubated in freshly prepared 5% potassium ferrocyanide (Sigma-Aldrich) solution (Perl's stain) with 10% hydrochloric acid for 20 min, rinsed and then counterstained with 0.1% nuclear fast red solution (Sigma-Aldrich) for 5 min. The tumour slices were dehydrated again through 95% and 2 changes of 100% ethanol and cleared in xylene and the coverslip was mounted with DPX (distyrene, plasticiser and xylene, Sigma-Aldrich). Images of the tumour slices were taken using a slide scanner (Nanozoomer, Hamamatsu, Japan).

2.3.5. Direct iron quantification by ferrozine assay

To validate MR imaging results, mice were sacrificed and the subcutaneous tumours were removed; 2 mL Lysing matrix D tubes containing tissue homogeniser beads were purchased from BP Biomedicals (Santa Ana, California, USA). The tumour samples were placed in the lysing tubes and a high-speed benchtop reciprocating homogeniser (Fastprep-24™ Sample Preparation Instrument, MP Biomedicals) was used to homogenise the tissue samples. 50 mg of each tissue sample was transferred to a 1.5 mL test tube, 100 μL of 0.6 M hydrochloric acid was added to each sample and the samples were incubated in a heat block at 65 °C for 2 h. 30 μL of pre-made ferrozine reagent was then added to the samples and the absorbance was measured at 570 nm using a benchtop spectrophotometer (Multiskan™ FC microplate photometer, Thermo scientific). The same procedure was carried out for serial dilutions of known amounts of fluidMag-CT particles to allow calibration (as described in Section 2.2.2). The results of the two tumour groups (Targeted and non-targeted) were statistically tested using non-parametric Mann-Whitney test.

3. Results

3.1. Effect of the particle size and force homogeneity on magnetic capturing

The ability to capture individual magnetic particles, and as such a therapy, depends on magnetic force, which is contingent on magnet design, the distance between the magnet and the particle, and the size and magnetic properties of the particle. To investigate these, we used a flow phantom to magnetically capture nanoparticles at various distances, flow velocities, and particle sizes (50 and 100 nm) using different magnet designs. We simulated the magnitude and spatial distribution of the magnetic field strength for the three designs (Supplementary Figs. 1–3). We then calculated the strength of the magnetic force (denoted as $|(B.\nabla)B| \approx$ B.gradB value, see Supplementary information) at these spatial locations around each magnet (Supplementary Fig. 4).

When targeting using the disk magnet we observed that 100 nm particles were readily attracted to the capillary tube wall (Fig. 1A red arrow), at clinically relevant tumour flow velocities [31–33] (5, 8, 10 mms^{-1}) and distances from the magnet edge (0, 3, 6, 8 mm) (Fig. 1B,C). As expected, capturing efficiency decreased with increasing distance from magnet edge as well as flow velocity (e.g. at 5 mms^{-1}

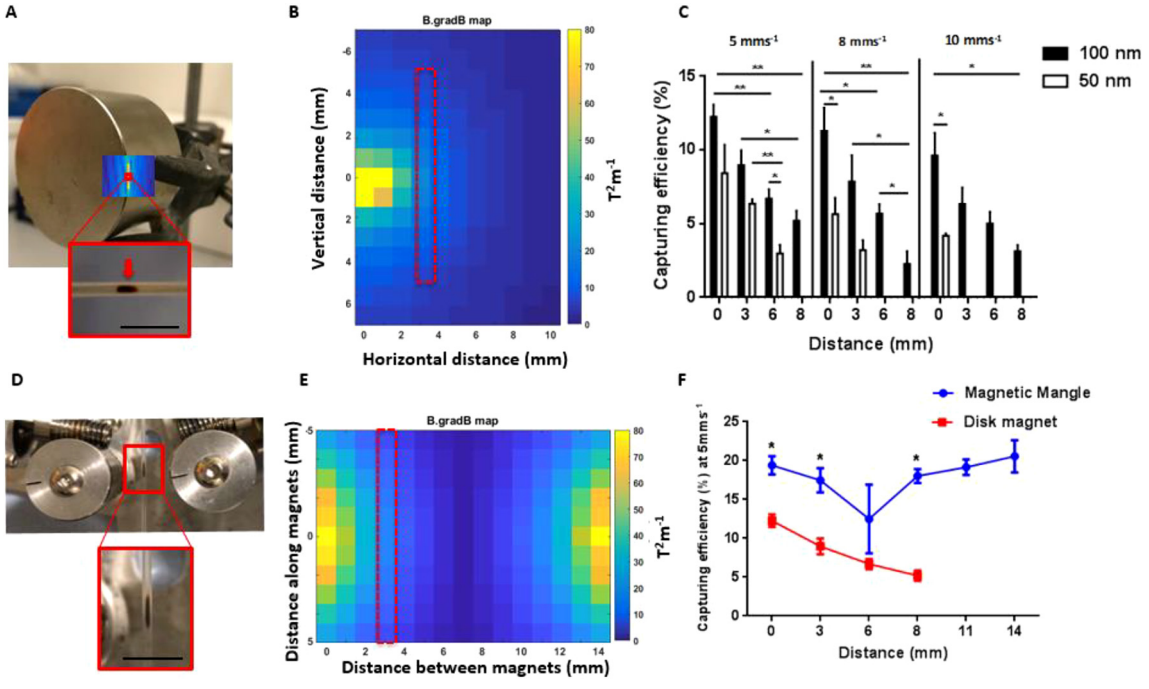

Fig. 1. Magnetic targeting of nanoparticles in a flow phantom. (A) Experimental set up showing tubing with the accumulated nanoparticles flowing past the edge of the disk magnet, scale bar 10 mm. (B) The B.gradB map (T^2m^{-1}) of the disk magnet in the plane moving away from the edge and at 30° from the circular face of the magnet where the tubing was positioned. The direction of the vector field is towards the magnet edge. (C) Capturing efficiency of accumulated particles (100 nm or 50 nm size) at three flow velocities and four distances from the magnet measured with quantitative ferrozine assay; mean ± SEM ($^*P < 0.05$, $n = 3$). (D) Experimental set-up showing tubing with the accumulated nanoparticles flowing past within the magnetic mangle, scale bar 10 mm. (E) The B.gradB map (T^2m^{-1}) of the magnetic mangle in the plane between the two magnets where the tubing was positioned. The direction of the vector field is towards the surface of each magnet. For ease of comparison with the B.gradB map of the disk magnet, the distance between two magnets has been measured with respect to one of the magnets (magnet on the left) rather than the centre plane between two magnets. (F) Capturing efficiency of accumulated 100 nm particles at 5 mms^{-1} flow velocity and 6 distances produced by the disk and mangle magnet designs; mean ± SEM ($^*P < 0.05$, n = 3).

flow velocity, capturing efficiency at 0, 3, 6 and 8 mm was 12.3 ± 0.6%, 8.9 ± 0.8%, 6.7 ± 0.5% and 5.3 ± 0.5%, respectively). Nanoparticle capturing at 0 mm distance was observed to be 2.4-fold higher ($n = 3$, $^{**}P < 0.025$) than 8 mm distance at the same flow velocity. Additionally, considering the effect of flow velocity, the capturing efficiencies at 0 mm distance were 12.3 ± 0.6%, 11.3 ± 1.3% and 9.6 ± 1.3% for flow velocities of 5, 8 and 10 mms^{-1} respectively.

When repeated with 50 nm sized particles, magnetic capturing was only possible ≤6 mm away from the magnet at 5 mms^{-1} velocity, ≤6 mm at 8 mms^{-1} and only 0 mm at 10 mms^{-1}. We observed a significant difference between capturing efficiency of 100 nm and 50 nm particles at 6 mm distance when flowing at our lowest flow (5 mms^{-1}) and at 0 mm distance when flowing at 8 and 10 mms^{-1} ($n = 3$, $^{*}P < 0.05$).

To investigate capturing with the magnetic mangle, the flow phantom experiment was repeated on 100 nm particles and at the same flow velocities as the disk magnet. Compared to the conventional disk magnet, the magnetic mangle produces a larger region of space with substantial magnetic field gradients. For example, the sum of B.gradB values in the vertical direction at 3 mm distance (dashed area, Fig. 1B, E) from the mangle (212 T^2m^{-1}) was found to be 1.6-fold higher than the corresponding value for the disk magnet (133 T^2m^{-1}). The tubing was placed between the two magnets (Fig. 1D, Supplementary Fig. 5) at distances of 0–14 mm. Capturing efficiency was markedly increased compared to the disk magnet at 0, 3 and 8 mm distances when flowing at 5 mms^{-1} ($n = 3$, $^{*}P < 0.05$, Fig. 1F). The capturing efficiency at 5 mms^{-1} and 3 mm distance (17.3 ± 1.3%) was observed to be 1.9-fold higher than the corresponding value for the disk magnet experiments (8.9 ± 0.8%). Interestingly, the difference in capturing efficiency between the two magnets was similar to the 1.6-fold difference in the B.gradB generated by the magnets. Due to the design of the pyramid magnet similar experiments could not be performed for comparison.

In order to decide which particle size to take forward to in vivo experiments, we noted that both the disk and mangle magnets, were readily able to capture 100 nm particles at our maximum flow velocity (10 mms^{-1}) and 8 mm distance (B.gradB values were 3 and 4 T^2m^{-1} respectively). As such, the 100 nm particles were taken forward as targeting at 8 mm or less would provide total coverage of a subcutaneous tumour.

3.2. Disk magnet - in vivo targeting and imaging

Next we used quantitative MRI to investigate targeting of 100 nm particles to tumours in vivo. We observed marked magnetic targeting of nanoparticles to tumours on the MR images as hypointense regions (decreased T_2^*) within the tumours (circled, Fig. 2A). Quantitative T_2^* maps (overlaid onto anatomical T_2-weighted images, Fig. 2B) give a clear indication as to the extent and spatial distribution of nanoparticle accumulation in the targeted tumour. T_2^* was markedly reduced in the targeted tumours ($n = 6$, $^{*}P < 0.05$, Fig. 2C) when using the disk magnet, while the non-targeted tumour did not change. To validate the MR imaging results, a quantitative ferrozine assay measurement was carried out on homogenised tumour tissues. The assay showed a higher concentration of nanoparticles in the targeted tumour tissue compared to non-targeted controls ($n = 4$, $^{*}P < 0.05$, Fig. 2D).

Investigating the spatial distribution more closely, we observed more T_2^* hypo-intense regions in locations closest to the magnet (Fig. 2F, red

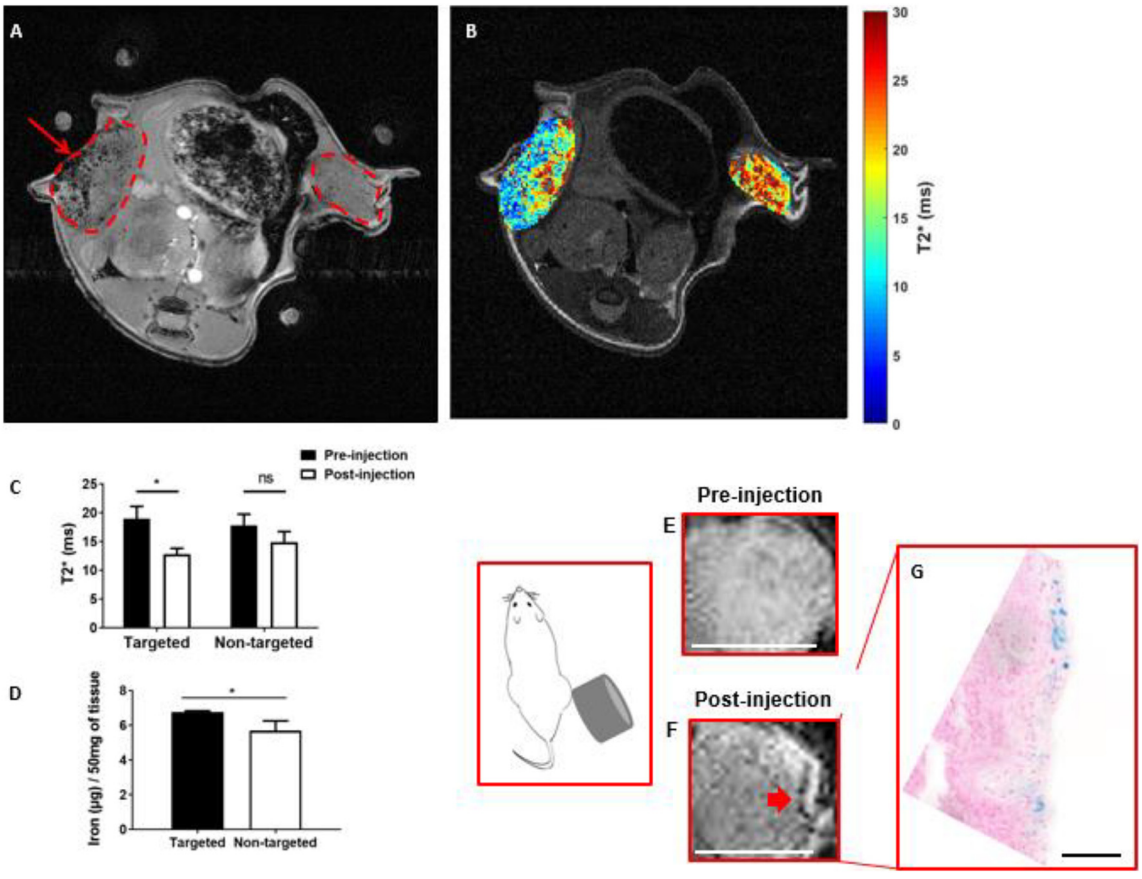

Fig. 2. In vivo magnetic targeting of nanoparticles using the disk magnet (A) T_2^*-weighted MR image showing bilateral subcutaneous tumours (circled) with hypointense regions in tumour exposed to external magnetic field (left) during and after intravenous nanoparticle injection; homogenous MR signal in non-targeted tumour (right). (B) T_2^* map of same tumours overlaid on T_2-weighted image indicating spatial distribution of T_2^* reduction as a consequence of nanoparticle accumulation. (C) In vivo magnetic targeting using the disk magnet design significantly reduces mean T_2^* after injection of nanoparticles ($^{*}P < 0.05$, $n = 6$). (D) Magnetic targeting significantly increases iron measurement in the tumour indicated by quantitative ferrozine assay; mean ± SEM ($^{*}P < 0.05$, $n = 4$). (E) Subcutaneous tumour prior to nanoparticle injection; Scale bar 5 mm (F) Same tumour after magnetic targeting of nanoparticles. (G) Nanoparticle accumulation confirmed by Perl's Prussian blue histology. Scale bar 100 μm.

arrow), which were not present prior to injection of nanoparticles and magnetic targeting (Fig. 2E). Prussian blue staining of ex vivo tissue samples provided further confirmation of iron in the proximal region of the tumour (Fig. 2G).

3.3. Mangle and pyramid magnets - in vivo targeting and imaging

To investigate in vivo targeting of tumours exposed to a larger magnetically active space, we performed further in vivo experiments using the mangle and pyramid magnet designs (Fig. 3A, B).

We observed a significant reduction in the T_2^* of the tumour tissues targeted with both the magnetic mangle ($n = 6$, $^*P < 0.05$) and pyramid magnet ($n = 6$, $^*P < 0.05$) designs. In the contralateral control tumour, the tumour T_2^* did not change after injection of nanoparticles (Fig. 3A, B, Supplementary Fig. 7A, B). Linear regression analysis revealed a significant correlation between the percentage enhancement in iron measurement of the ferrozine assay and the T_2^* reduction of the targeted tumours ($r^2 = 0.9635$, $^*P < 0.05$, Supplementary Fig. 7C).

Three-dimensional reconstructions display the nanoparticle distribution within the targeted (Fig. 3C) and non-targeted (Fig. 3D) tumours. Hypointensities can be observed throughout the whole volume of the targeted tumour and are not confined to the region closest to the magnet, consistent with the strong force experienced by the nanoparticles from the pyramid magnet over the whole tumour (Supplementary Fig. 4E, F).

3.4. Effect of larger magnetically active space – in vivo targeting distribution

The ideal magnet design would apply a sufficiently strong magnetic force throughout the whole tumour. As such we took a quantitative approach to compare our 3 magnet designs. We investigated the spatial distribution of nanoparticles within the tumours quantitatively by measuring the T_2^* values across tumours (1 to 4 mm within each tumour) before and after nanoparticle administration (Fig. 4A–C). We further performed linear regression analysis on the post-injection T_2^* values to investigate whether the slope of T_2^* deviates from zero as we move deeper within the tumour.

Investigating the magnets individually: i) *Disk magnet*, we observed an increasing trend in post-injection T_2^* of the targeted tumours. The slope of the post-injection T_2^* was different from zero ($n = 6$, $^*P < 0.05$, Fig. 4A) and as expected, the further away from the magnet, the less targeting was observed. ii) *Mangle design*, we found a similar increasing trend in post-injection T_2^* of the targeted tumours, presumably as the tumour was located close to one of the magnets. The slope of the post-injection T_2^* was different from zero ($n = 6$, $^*P < 0.05$, Fig. 4B) iii) *Pyramid magnet*, T_2^* of tumours targeted showed no change in T_2^* with respect to distance. No deviation from zero was observed on the slope of the post-

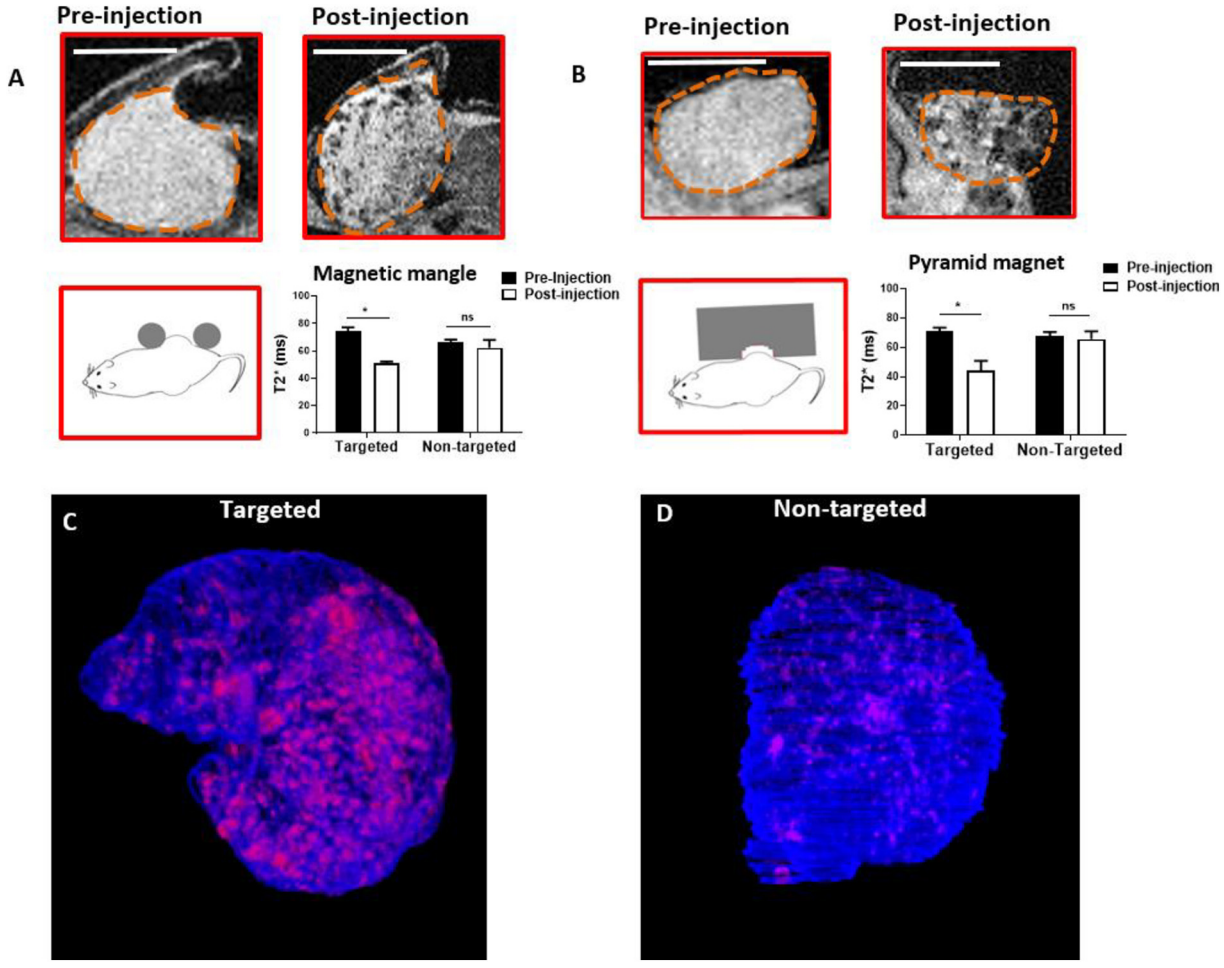

Fig. 3. In vivo magnetic targeting of nanoparticles using the mangle and pyramid magnets. (A) In vivo magnetic targeting using the magnetic mangle design. The figure shows the ROIs of the pre and post injection for targeted tumours. Scale bars 5 mm. Magnetic targeting significantly reduces the mean tumour T_2^* after injection of magnetic nanoparticles; mean ± SEM ($^*P < 0.05$, $n = 6$). (B) In vivo magnetic targeting using the pyramid magnet design. The figure shows the ROIs of the pre and post injection for targeted tumours. Scale bars 5 mm. Magnetic targeting significantly reduces the mean tumour T_2^* after injection of magnetic nanoparticles; mean ± SEM ($^*P < 0.05$, $n = 6$) (C) Three-dimensional reconstructed image from a tumour targeted using the pyramid magnet and the contralateral non-targeted tumour (D). Segmented hypointense regions are shown in red. (For interpretation of the references to colour in this figure legend, the reader is referred to the web version of this article.)

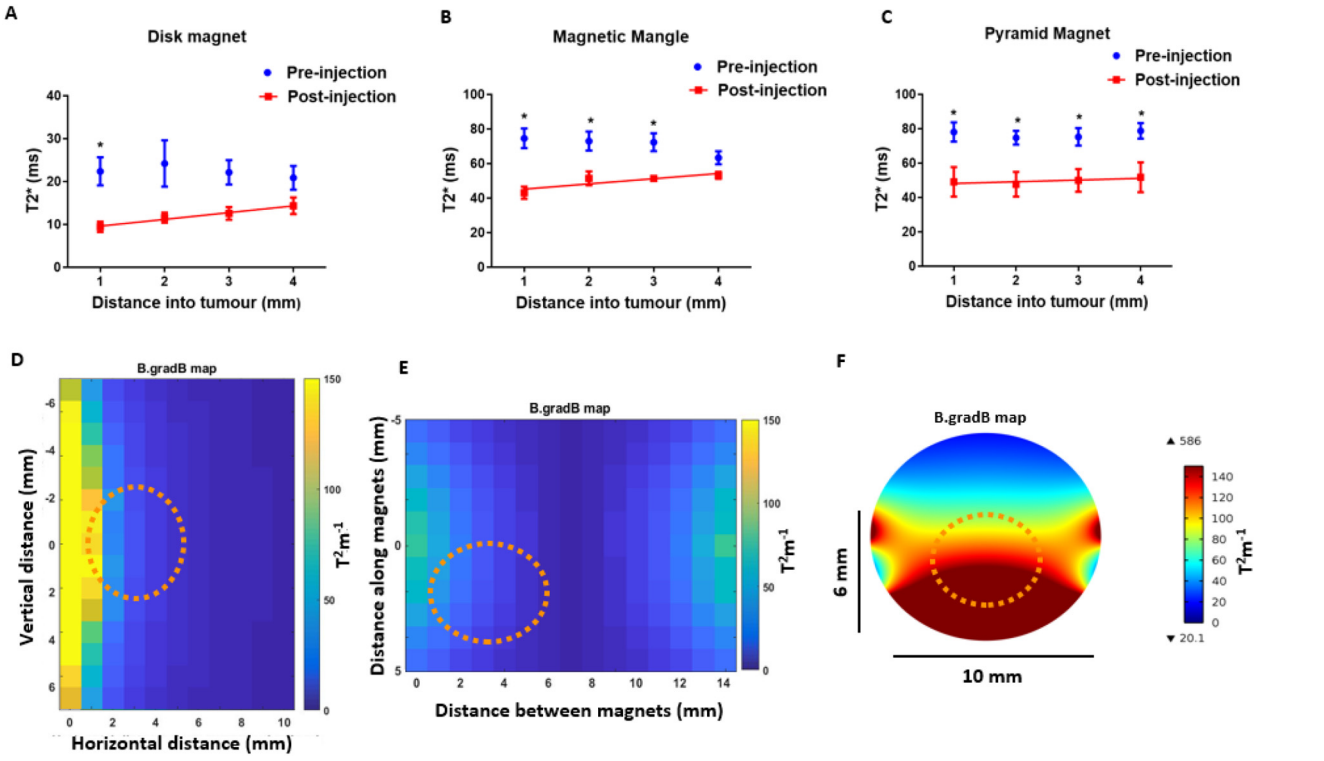

Fig. 4. Effect of magnetically active space on magnetic tumour targeting. The spatial T_2* distribution of the magnetically targeted tumours pre and post nanoparticle injection using the three magnet designs (A) The disk magnet; mean ± SEM ($n = 6$). (B) The magnetic mangle; mean ± SEM (n = 6). (C) The pyramid magnet; mean ± SEM (n = 6). B.gradB topography of the three magnet designs on the same colour threshold. The approximate tumour position is shown in each map (D) The disk magnet. The direction of the vector field is towards the magnet edge. (E) The magnetic mangle. The direction of the vector field is towards the magnet surfaces. (F) The pyramid magnet. The direction of the vector field is towards the closest magnet surface.

injection T_2* line ($n = 6$, $P = 0.9117$, Fig. 4C). As such, it can be concluded that the pyramid magnet produces the most uniform and most homogeneous targeting within tumours.

In order to compare the spatial distribution of nanoparticle accumulation with the magnetic force applied by each magnetic design, the force (denoted by the B.gradB map) generated by each magnet, and the approximate tumour position within each map are shown in a two dimensional plot (Fig. 4D–F). The B.gradB magnitude at a distance of 6 mm away from the disk magnet (6 T^2m^{-1}) was similar to the corresponding value generated by one of the cylindrical magnets in the mangle design (5 T^2m^{-1}). The sharp decline in the magnitude of the applied force, accounts for the reduction in targeting at deeper locations of the tumour. Conversely, the pyramid magnet generates considerably larger B.gradB (>90 T^2m^{-1}) across the tumour volume, consistent with the observed homogenous targeting within the tumours.

3.5. Translation of magnet design from mouse to human

In order to target individual nanoparticles at distances similar to human proportions, we aimed to translate our scalable magnets into larger dimensions. The ideal external magnet would have a magnetically active space large enough to accommodate a part of human body and strong enough to target nanoparticles in human tumours. The flow phantom experiments showed that the minimum B.gradB value, which allowed capturing of 100 nm particles against flow was 3 T^2m^{-1}. As such, we used mathematical modelling in accordance with Nacev-Shapiro magnetic targeting construct (see supplementary information) to confirm that this B.gradB magnitude is large enough to capture 100 nm particles in human blood vessels. We adopted the blood and blood vessel parameters in humans from the Lubbe et al. clinical study [1], as reported in Nacev et al. [31] and Al-Jamal et al. [24]. The results of these calculations predict a boundary layer formation regime, which indicates successful magnetic targeting (Supplementary Fig. 8).

We then worked with Giamag magnet company to design a scaled-up pyramid magnet, which generates a minimum B.gradB value of 3 T^2m^{-1} (threshold value). The threshold value generated by the magnet decreases with increasing the size of the magnetically active space. As such we employed the high magnetic gradient design [35] of the pyramid magnet to develop a magnet with a magnetically active space that generates the threshold strength value, and is readily constructed. Finite element modelling and simulations resulted in a U-shaped magnet design, which contains a magnetically active space of 10 cm long, 7 cm deep and 7 cm wide, equivalent to a total volume of 490 cm^3 (Fig. 5A), producing a feasible solution for capturing chemotherapy agents in the breast, neck, leg, and other body organs with similar sizes. The maximum depth at which the threshold B.gradB value is generated is in the range of 5–7 cm from the bottom surface of the magnetically active space depending on the position with respect to the X-axis of the magnet (Fig. 5B). The direction of the magnetic force is pointing towards the nearest magnet surface at any point within the magnetically active space (Fig. 5C). These data confirm that the high magnetic gradient design of the pyramid magnet can be scaled-up with suitable strength and dimension for the clinical setting.

4. Discussion

Magnetic drug targeting offers a promising method to increase delivery of chemotherapeutic agents to tumours while reducing the systemic dosing of the drug. However, it is still unclear whether it will be possible to target SPIONs to tissues deeper in the body [19,24]. This study reports marked magnetic targeting of magnetic nanoparticles to tumours using novel custom-made permanent magnetic designs, which have a clinical end-point in mind. These magnets were designed to target a specific volume of tissue, known as the 'magnetically active space', where agents can be delivered. We have demonstrated that our bespoke permanent magnet can target nanoparticles at deeper

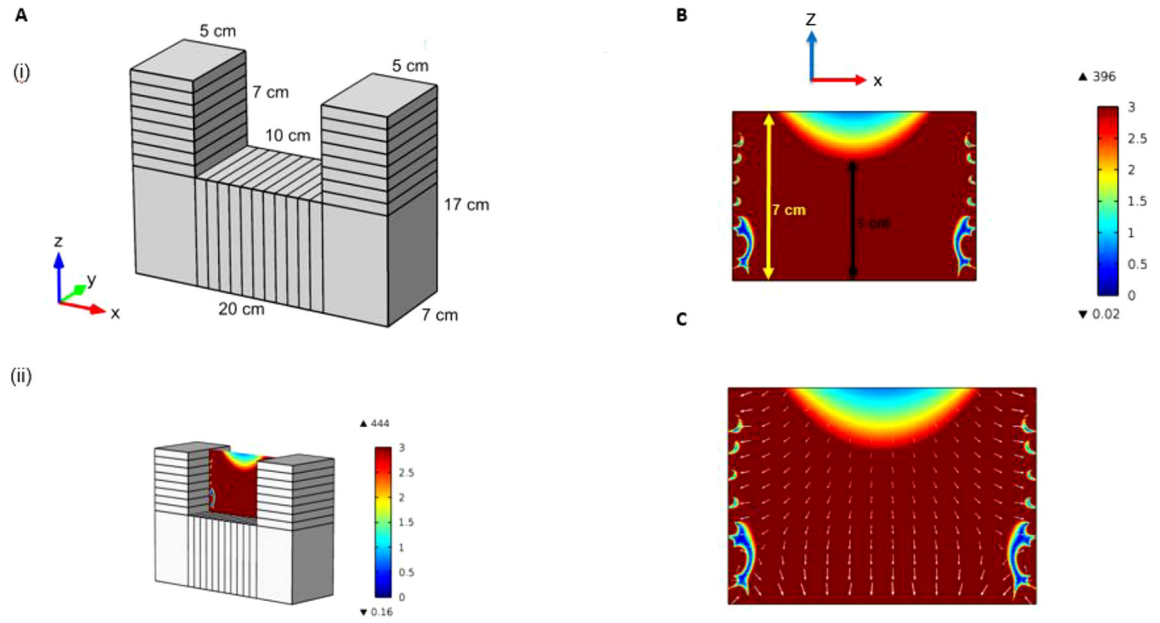

Fig. 5. The scaled-up magnet design. (A) (i) The magnet shape and dimensions. (ii) The B.gradB plane within the magnetically active space. (B) The B.gradB map of the magnetically active space with a colour scale threshold of 3 T^2m^{-1}. (C) The vector field map of the B.gradB in the same plane. The direction of the vector field is towards the closet magnet surface.

tumour locations in comparison to a traditional disk magnet, while delivering a more homogenous distribution of nanoparticles throughout the tumour. Based on the improved targeting capacity of the pyramid magnet, we provide designs for a scaled-up magnet potentially capable of targeting 100 nm particles up to a depth of 7 cm within specific locations of the human body.

During recent years, a considerable amount of research has focused on developing hybrid magnetic nanoparticles such as SPION-loaded solid lipid nanoparticles [36,37], SPION-loaded polymeric nanoparticles [38], and nano-worm structures [39]. These complex systems provide a biocompatible capsulation, which aid the auto accumulation of the drug in the tumour tissue due to the EPR effect. Additionally, some of these nanostructures have shown to be effective in penetrating through BBB to deliver drug to the brain [40], allowing a higher cytotoxic concentration at the tumour site and a reduced toxicity in healthy cells. Previous in vitro [41,42] and preclinical magnetic targeting studies [43,44] were performed using nanoparticles in association with chemotherapy drugs in a wide range of brain tumour models, including GBM. This study builds on these investigations by proposing magnet designs which may increase SPION-labelled nanoparticles to a tumour site. In addition to drug delivery, the proposed solution in this study may be highly beneficial in magnetic hyperthermia applications, in which the main challenge is to obtain a sufficiently high concentration of nanoparticles in the tumour to result in useful heating at clinically tolerable levels of alternating magnetic fields [11,45]. Increasing nanoparticle accumulation in tumours post systemic or local administration using the methods developed in this study may provide a potential solution to this challenge.

Although the rapidly emerging field of nanotechnology has led to production of magnetic nanoparticles with desirable properties in a variety of biomedical applications, some research suggest that these particles can cause a reactive oxygen species (ROS)-induced oxidative stress on certain cell types [46], which could initiate undesirable pathophysiological outcomes such as genotoxicity, inflammation, fibrosis, and carcinogenesis [47]. Even though the overall toxicity profile of iron oxide nanoparticles is not well understood [48], particles have been used routinely in patients for diagnostic and therapeutic purposes (for example Feraheme® in iron deficiency anaemia [49]), without causing notable toxicity. In addition, magnetic drug targeting of iron oxide nanoparticles conjugated with chemotherapeutic agent was reported to be safe and well tolerated in the phase one clinical study [1]. Further work is needed to understand the toxicity mechanisms of these nanoparticles at a cellular level, which may yield novel strategies to mitigate potential short and long term risks in the future.

In this study we observed a marked difference in capturing efficiency between the 50 and 100 nm particles when performing the in vitro targeting experiments. Reducing the size of nanoparticle may lead to improved penetration of nanoparticles into tumours, but appears offset by the lack of applied targeting force. Multiple studies using 100 nm particles have reported considerable accumulation of this particle size within the tumour [1,21,26,33]. Importantly, having a 100 nm particle with a multi-domain core increases the magnetic force substantially when compared to single core 50 or 20 nm particles, therefore, aiding the tumour penetration. As such, it was determined that 100 nm particles were more suitable for in vivo magnetic targeting experiments.

Evidence suggests that targeting of SPIONs with traditional permanent magnets is limited to <5 mm into the human body [1,24]. Using our magnetic mangle design, composed of two magnets on either side of the targeting region, we show that capturing depth is almost double (14 mm) that of the traditional disk magnet (8 mm). Moreover, improved capturing efficiency was observed throughout the entire targeting region of the mangle compared to the disk magnet, highlighting the need for designing magnets with a large magnetically active space. This led to the development of the pyramid magnet, designed to deliver a strong magnetically active space that would encompass the total volume of the subcutaneous tumours. Unlike previous custom-made electro and permanent magnets for magnetic nanoparticle targeting [26,32] the pyramid magnet is readily scalable to human size proportions.

We investigated in vivo magnetic targeting of individual 100 nm particles to subcutaneous tumours and utilised MRI to non-invasively quantify particle delivery. As shown previously in glioma tumour models [26], a reduction of T_2^* was observed in magnetically targeted tumours while no significant change was observed in the contralateral control tumour. While Chertok et al noted homogenous hypo-intensities in their MR images, we observed discrete patches of hypo-intense regions distributed across the tumour tissue. This is likely the result of the difference in passive delivery of nanoparticles between the two tumour models as the glioma model used in the previous reports has about 4.5-fold higher capillary blood perfusion [33,50] compared with the tumour model used in this study [51]. The discrete regions of hypointensities observed

in this study allowed for the spatial mapping of targeted particles using MRI. When targeting was performed using the pyramid magnet, hypo-intense patches were observed throughout the whole tumour region with significant T_2^* reduction at all tumour depths (≤4 mm). Conversely, using the disk magnet hypo-intensities were only observed at locations close to the magnet with T_2^* reduction only significant at a depth of 1 mm. These results are consistent with the bespoke pyramid magnet having a magnetically active space covering the entire tumour volume. Previously, Chertok et al. [52] created a modified electromagnet setup, which exhibits an improved magnetic field gradient across the tumour region over their standard electromagnet design. Compared to the B.gradB value produced by this modified electromagnet setup (14.4 T^2/m), the pyramid magnet produces a minimum of 6 times higher strength (90 T^2/m) across the targeting region, which increases the likelihood of nanoparticle entrapment during their passage through the circulation.

Magnetic drug targeting has been demonstrated in animals and human patients, but its utility has been limited to shallow targets. The first clinical trial demonstrated efficacy of this technique in superficial tumours, which were located up to a depth of 5 mm from the skin in head, neck and breast cancers [1]. Here, we have investigated minimum gradients required to capture 100 nm particles in human blood vessels (supplementary information) and have designed a scaled-up U-shaped permanent magnet capable of delivering these gradients. One cancer treatment which would specifically benefit from our developed magnet design is breast cancer, where single or multiple tumours are located within the breast tissue. Previous studies have demonstrated the efficacy of surface functionalised drug conjugated magnetic nanoparticles in breast tumour suppression and reducing systemic toxicity of drugs [53,54]. In addition to the selective accumulation of magnetic nanoparticles in tumours, the present study also shows that introduction of an external magnetic field can significantly enhance such delivery, which is in agreement with previous reports [24,26,55]. Additionally, our study provides the potential to substantially increase achievable targeting depth of traditional permanent magnets from 5 mm to 7 cm distance into the breast or body organs with similar sizes such as neck or legs. It has to be noted that generating such magnetic gradients at centimetre distance scales is remarkable. To our knowledge, the most optimised permanent magnetic system designed for magnetic drug targeting [56] is capable of producing B.gradB values of about 0.3 T^2/m at 5 cm distance from the magnet. Our scaled-up magnet can generate a minimum B.gradB value of 3 T^2/m at the same distance, delivering a 10-fold higher magnetic force.

In this study, two magnetic devices were developed, generating a larger magnetic exposure in comparison to a traditional disk magnet. Magnetic targeting of nanoparticles was then investigated using these magnet designs both in vitro and in vivo. In summary, our results suggest that compared to the traditional disk magnet, our bespoke magnet design produces more homogenous and deeper nanoparticle distribution within the tumour. Using theoretical simulations, we have shown that our magnetic setup can be extrapolated to target 100 nm particles in tumours located up to 7 cm depth at specific locations of human body. To the best of our knowledge, this is the first study to report magnetic tumour targeting of nanoparticles using custom-made, strong and scalable magnetic designs.

Author contributions

Conception and design, MFL, MM, JJC, PSP.; Development of methodology, MFL, MM, JJC, PSP.; Data acquisition, MM, JJC.; Resources, MFL.; Analysis and interpretation of data, MM, JJC, BS.; Writing of manuscript, MM, JJC, MFL, PSP, CP.; Review and revision of manuscript, MM, MFL, JJC, PSP, CP, QAP, TK, YY, RB.; Project supervision, MFL, QAP.

Data availability

The raw/processed data required to reproduce these findings cannot be shared at this time due to technical or time limitations.

The raw/processed data are available upon request.

CRediT authorship contribution statement

Matin Mohseni: Conceptualization, Data curation, Formal analysis, Funding acquisition, Project administration, Writing - original draft, Writing - review & editing. **John J. Connell:** Conceptualization, Data curation, Formal analysis, Funding acquisition, Supervision, Writing - review & editing. **Christopher Payne:** Writing - review & editing. **P. Stephen Patrick:** Conceptualization, Funding acquisition, Writing - review & editing. **Rebecca Baker:** Writing - review & editing. **Yichao Yu:** Writing - review & editing. **Bernard Siow:** Resources. **May Zaw-Thin:** Data curation. **Tammy L. Kalber:** Writing - review & editing. **Quentin A. Pankhurst:** Supervision, Writing - review & editing. **Mark F. Lythgoe:** Conceptualization, Formal analysis, Funding acquisition, Supervision, Writing - review & editing.

Declaration of competing interest

Authors declare no competing interests.

Acknowledgments

The authors would like to thank Daniel Hochhauser for helpful theoretical discussion and May Zaw-Thin for assistance during intravenous injections and preparing the DLS and TEM data.

ML receives funding from the EPSRC (EP/N034864/1); the King's College London and UCL Comprehensive Cancer Imaging Centre CR-UK & EPSRC, in association with the MRC and DoH (England); UK Regenerative Medicine Platform Safety Hub (MRC: MR/K026739/1); Brain Tumour Charity; MM was self-funded PhD student.

PSP received funding from MRC grants MR/R026416/1 and MR/K026739/1.

TK receives funding from EPSRC Early Career Fellowship (EP/L006472/1).

The funds required to produce the proof of concept magnets were provided by Centre for Advanced Biomedical Imaging (CABI) in UCL.

This research did not receive any specific grant from funding agencies in the public, commercial, or not-for-profit sectors.

Appendix A. Supplementary data

Supplementary data to this article can be found online at https://doi.org/10.1016/j.matdes.2020.108610.

References

[1] B.C. Lübbe AS, H. Riess, F. Schriever, P. Reichardt, K. Possinger, M. Matthias, B. Dörken, F. Herrmann, R. Gürtler, P. Hohenberger, N. Haas, R. Sohr, B. Sander, A.J. Lemke, D. Ohlendorf, W. Huhnt, D. Huhn, Clinical experiences with magnetic drug targeting: a phase I study with 4′-epidoxorubicin in 14 patients with advanced solid tumors, Cancer Res. 56 (20) (Oct. 1996) 4686–4693.

[2] M.W. Wilson, et al., Hepatocellular carcinoma: regional therapy with a magnetic targeted carrier bound to doxorubicin in a dual MR imaging/conventional angiography suite—initial experience with four patients, Radiology 230 (1) (2004) 287–293Jan.

[3] E.E. Estelrich, J. Queralt, M.A. Busquets, Iron oxide nanoparticles for magnetically-guided and magnetically-responsive drug delivery, Int. J. Mol. Sci. 2015 (16) (2015) 8070–8101.

[4] K.D.L. Johannes Riegler, Ana Garcia-Prieto, Anthony N. Price, Toby Richards, Quentin A. Pankhurst, M.F. Lythgoe, Magnetic cell delivery for peripheral arterial disease: a theoretical framework, Med. Phys. 38 (7) (2011)Jul.

[5] P.P. Connell JJ, Y. Yu, M.F. Lythgoe, T.L. Kalber, Advanced cell therapies: targeting, tracking and actuation of cells with magnetic particles, Regen. Med. 10 (6) (2015) 757–772.

[6] L.P. Kyrtatos, M. Junemann-Ramirez, A. Garcia-Prieto, A.N. Price, J.F. Martin, D.G. Gadian, Q.A. Pankhurst, M.F. Lythgoe, Magnetic tagging increases delivery of circulating progenitors in vascular injury, JJACC Cardiovasc Interv. 2 (8) (2009) 794–802.

[7] E.K.J. Ali, S. Arbab, Lindsey B. Wilson, Gene T. Yocum, Bobbi K. Lewis, Joseph A. Frank, In vivo trafficking and targeted delivery of magnetically labeled stem cells, Hum. Gene Ther. 15 (4) (2004) 351–360.

[8] Q.A.P.P. Stephen Patrick Christopher Payne, Tammy L. Kalber, Mark F. Lythgoe, Magnet-targeted delivery and imaging, Design and Applications of Nanoparticles in Biomedical Imaging 2016, pp. 123–149.
[9] P.G.K.R.A. Panizzo, A.N. Price, D.G. Gadian, P. Ferretti, M.F. Lythgoe, In vivo magnetic resonance imaging of endogenous neuroblasts labelled with a ferumoxide-polycation complex, Neuroimage 44 (4) (Feb. 2009) 1239–1246.
[10] D.L.K.J.W. Bulte, Iron oxide MR contrast agents for molecular and cellular imaging, NMR Biomed. 17 (7) (2004) 484–499.
[11] K.L.O. Tammy, L. Kalber, Paul Southern, Michael R. Loebinger, Panagiotis G. Kyrtatos, Quentin A. Pankhurst, Mark F. Lythgoe, Sam M. Janes, Hyperthermia treatment of tumors by mesenchymal stem cell-delivered superparamagnetic iron oxide nanoparticles, Int. J. Nanomedicine 11 (2016) (2016) 1973–1983.
[12] G. von Maltzahn, A.M. Derfus, T.J. Harris, T. Duza, K.S. Vecchio, E. Ruoslahti, Remotely triggered release from magnetic nanoparticles, Adv. Mater. 19 (22) (2007) 3932–3936.
[13] G.K. Thirunavukkarasu, K. Cherukula, H. Lee, Y.Y. Jeong, I.-K. Park, J.Y. Lee, Magnetic field-inducible drug-eluting nanoparticles for image-guided thermo-chemotherapy, Biomaterials 180 (2018) 240–252Oct.
[14] M.F.K. Enming Zhang, Martin Koch, Lena Eliasson, S. Nahum Goldberg, Erik Renström, Dynamic magnetic fields remote-control apoptosis via nanoparticle rotation, ACS Nano 8 (4) (2014) 3192–3201.
[15] D.M. Ganeshlenin Kandasamy, Recent advances in superparamagnetic iron oxide nanoparticles (SPIONs) for in vitro and in vivo cancer nanotheranostics, Pharmaceutics 496 (2015) 191–218.
[16] J. Riegler, et al., Superparamagnetic iron oxide nanoparticle targeting of MSCs in vascular injury, Biomaterials 34 (8) (2013) 1987–1994Mar.
[17] J. Cores, T. Caranasos, K. Cheng, Magnetically targeted stem cell delivery for regenerative medicine, Journal of Functional Biomaterials 6 (3) (2015) 526–546Jun.
[18] S. Lyer, R. Singh, R. Tietze, C. Alexiou, Magnetic nanoparticles for magnetic drug targeting, Biomedical Engineering/Biomedizinische Technik 60 (5) (2015)Jan.
[19] B. Shapiro, S. Kulkarni, A. Nacev, S. Muro, P.Y. Stepanov, I.N. Weinberg, Open challenges in magnetic drug targeting: open challenges in magnetic drug targeting, Wiley Interdisciplinary Reviews: Nanomedicine and Nanobiotechnology 7 (3) (2015) 446–457May.
[20] F. Danhier, O. Feron, V. Préat, To exploit the tumor microenvironment: passive and active tumor targeting of nanocarriers for anti-cancer drug delivery, J. Control. Release 148 (2) (2010) 135–146Dec.
[21] A.J. Cole, A.E. David, J. Wang, C.J. Galbán, H.L. Hill, V.C. Yang, Polyethylene glycol modified, cross-linked starch-coated iron oxide nanoparticles for enhanced magnetic tumor targeting, Biomaterials 32 (8) (2011) 2183–2193Mar.
[22] H. Marie, et al., Superparamagnetic liposomes for MRI monitoring and external magnetic field-induced selective targeting of malignant brain tumors, Adv. Funct. Mater. 25 (8) (2015) 1258–1269Feb.
[23] L.J. Shao, X. Zheng, Y. Pan, Z. Wang, M. Zhang, Q.X. Chen, W.F. Dong, L. Chen, Janus 'nano-bullets' for magnetic targeting liver cancer chemotherapy, Biomaterials 100 (2016) (2016) 118–133May.
[24] K.T. Al-Jamal, et al., Magnetic drug targeting: preclinical in vivo studies, mathematical modeling, and extrapolation to humans, Nano Lett. 16 (9) (2016) 5652–5660Sep.
[25] H. Maeda, J. Wu, T. Sawa, Y. Matsumura, K. Hori, Tumor vascular permeability and the EPR effect in macromolecular therapeutics: a review, J. Control. Release 65 (1–2) (2000) 271–284Mar.
[26] M.B. Chertok, A.E. David, F.Q. Yu, C. Bergemann, B.D. Ross, et al., Iron oxide nanoparticles as a drug delivery vehicle for MRI monitored magnetic targeting of brain tumors, Biomaterials 2008 (29) (2008) 487–496.
[27] B.A.J. Riegler, R.J. Cook, M.F. Lythgoe, Q.A. Pankhurst, Magnetically assisted delivery of cells using a magnetic resonance imaging system, J. Phys. D 44 (5) (2011) 5001–5013.
[28] A.J.K. Munitta Muthana, Russell Hughes, Ester Fagnano, Jay Richardson, Melanie Paul, Craig Murdoch, Fiona Wright, Christopher Payne, Mark F. Lythgoe, Neil Farrow, Jon Dobson, Joe Conner, Jim M. Wild, Claire Lewis, Directing cell therapy to anatomic target sites in vivo with magnetic resonance targeting, Nat. Commun. 6 (8009) (2015)Aug.
[29] A. Nacev, et al., Dynamic inversion enables external magnets to concentrate ferromagnetic rods to a central target, Nano Lett. 15 (1) (2015) 359–364Jan.
[30] E.M. Cherry, P.G. Maxim, J.K. Eaton, Particle size, magnetic field, and blood velocity effects on particle retention in magnetic drug targeting: particle retention in magnetic drug targeting, Med. Phys. 37 (1) (2009) 175–182Dec.
[31] A. Nacev, C. Beni, O. Bruno, B. Shapiro, The behaviors of ferromagnetic nanoparticles in and around blood vessels under applied magnetic fields, J. Magn. Magn. Mater. 323 (6) (2011) 651–668Mar.
[32] L.E. Udrea, N.J.C. Strachan, V. Bădescu, O. Rotariu, An *in vitro* study of magnetic particle targeting in small blood vessels, Phys. Med. Biol. 51 (19) (2006) 4869–4881Oct.
[33] B. Chertok, A.E. David, Y. Huang, V.C. Yang, Glioma selectivity of magnetically targeted nanoparticles: a role of abnormal tumor hydrodynamics, J. Control. Release 122 (3) (2007) 315–323Oct.
[34] M.M. Tomayko, C.P. Reynolds, Determination of subcutaneous tumor size in athymic (nude) mice, Cancer Chemother. Pharmacol. 24 (3) (1989) 148–154Sep.
[35] A.T. Skjeltorp, P. Dommersnes, H. Høyer, New forceful magnetic bioseparation using GIAMAG magnet systems, MRS Advances 2 (24) (2017) 1297–1301.
[36] X. Zhu, et al., SPIO-loaded nanostructured lipid carriers as liver-targeted molecular T2-weighted MRI contrast agent, Quant Imaging Med Surg 8 (8) (2018) 770–780Sep.
[37] H. Abbas, H. Refai, N. El Sayed, Superparamagnetic Iron oxide–loaded lipid nanocarriers incorporated in thermosensitive in situ gel for magnetic brain targeting of clonazepam, J. Pharm. Sci. 107 (8) (2018) 2119–2127Aug.
[38] B. Wang, W. Wu, H. Lu, Z. Wang, H. Xin, Enhanced anti-tumor of Pep-1 modified superparamagnetic iron oxide/PTX loaded polymer nanoparticles, Front. Pharmacol. 9 (2019)Jan.
[39] C.E. Smith, et al., Worm-like superparamagnetic nanoparticle clusters for enhanced adhesion and magnetic resonance relaxivity, ACS Appl. Mater. Interfaces 9 (2) (2017) 1219–1225Jan.
[40] T. Cerna, M. Stiborova, V. Adam, R. Kizek, T. Eckschlager, Nanocarrier drugs in the treatment of brain tumors, Journal of Cancer Metastasis and Treatment 2 (10) (2016) 407Oct.
[41] C. Tapeinos, et al., Cell membrane-coated magnetic nanocubes with a homotypic targeting ability increase intracellular temperature due to ROS scavenging and act as a versatile theranostic system for glioblastoma multiforme, Advanced Healthcare Materials 8 (18) (2019), 1900612Sep.
[42] A. Grillone, et al., Nutlin-loaded magnetic solid lipid nanoparticles for targeted glioblastoma treatment, Nanomedicine 14 (6) (2019) 727–752Mar.
[43] H. Xin, X. Sha, X. Jiang, W. Zhang, L. Chen, X. Fang, Anti-glioblastoma efficacy and safety of paclitaxel-loading Angiopep-conjugated dual targeting PEG-PCL nanoparticles, Biomaterials 33 (32) (2012) 8167–8176Nov.
[44] A. Ambruosi, S. Gelperina, A. Khalansky, S. Tanski, A. Theisen, J. Kreuter, Influence of surfactants, polymer and doxorubicin loading on the anti-tumour effect of poly (butyl cyanoacrylate) nanoparticles in a rat glioma model, J. Microencapsul. 23 (5) (2006) 582–592Jan.
[45] Q.A. Pankhurst, N.T.K. Thanh, S.K. Jones, J. Dobson, Progress in applications of magnetic nanoparticles in biomedicine, J. Phys. D. Appl. Phys. 42 (22) (2009), 224001Nov.
[46] U.S. Gaharwar, R. Meena, P. Rajamani, Iron oxide nanoparticles induced cytotoxicity, oxidative stress and DNA damage in lymphocytes: Iron oxide nanoparticles toxicity in lymphocytes, J. Appl. Toxicol. 37 (10) (2017) 1232–1244Oct.
[47] A. Manke, L. Wang, Y. Rojanasakul, Mechanisms of nanoparticle-induced oxidative stress and toxicity, Biomed. Res. Int. 2013 (2013) 1–15.
[48] T. Kornberg, et al., Potential toxicity and underlying mechanisms associated with pulmonary exposure to iron oxide nanoparticles: conflicting literature and unclear risk, Nanomaterials 7 (10) (2017) 307Oct.
[49] D.W. Coyne, Ferumoxytol for treatment of iron deficiency anemia in patients with chronic kidney disease, Expert. Opin. Pharmacother. 10 (15) (2009) 2563–2568Oct.
[50] A.C. Silva, S.-G. Kim, M. Garwood, Imaging blood flow in brain tumors using arterial spin labeling, Magn. Reson. Med. 44 (2) (2000) 169–173Aug.
[51] A. d'Esposito, et al., Computational fluid dynamics with imaging of cleared tissue and of in vivo perfusion predicts drug uptake and treatment responses in tumours, Nature Biomedical Engineering 2 (10) (2018) 773–787Oct.
[52] B. Chertok, A.E. David, V.C. Yang, Brain tumor targeting of magnetic nanoparticles for potential drug delivery: effect of administration route and magnetic field topography, J. Control. Release 155 (3) (2011) 393–399Nov.
[53] S. Shakil, A. Hasan, S.R. Sarker, Iron oxide nanoparticles for breast cancer theranostics, Curr. Drug Metab. 20 (2018)Nov.
[54] J. Chen, et al., Reducible polyamidoamine-magnetic iron oxide self-assembled nanoparticles for doxorubicin delivery, Biomaterials 35 (4) (2014) 1240–1248Jan.
[55] S.D. Kong, et al., Magnetically vectored nanocapsules for tumor penetration and remotely switchable on-demand drug release, Nano Lett. 10 (12) (2010) 5088–5092Dec.
[56] L.C. Barnsley, D. Carugo, E. Stride, Optimized shapes of magnetic arrays for drug targeting applications, J. Phys. D. Appl. Phys. 49 (22) (2016), 225501Jun.